Arab J. Nucl. Sci. Appl., Vol. 56, 3, 7-16 (2023)

ISSN 1110-0451

Arab Journal of Nuclear Sciences and Applications

Web site: ajnsa.journals.ekb.eg

(E S N S A)

Theoretical Study on the Quantum Well Junction $CrI_3/CrGeTe_3$

S. Soliman*, Mohammed Moaied+

Department of Physics, Faculty of Science, Zagazig University, 44519 Zagazig, Egypt

ARTICLE INFO

Article history:

Received: 18th July 2022

Accepted: 19th Nov. 2022

Keywords:

CrI_3;

$CrGeTe_3$ Junction;

Magneto-Volume Spin Coupling;

High Electron Mobility.

ABSTRACT

Electronic structure calculations were conducted for the CrI3/CrGeTe3 junction with different separations (z) between the two slabs, CrI3 and CrGeTe3, which provide a means to resolve the magneto-volume spin coupling. The calculations demonstrate that high electron mobility, high frequency, and strongly electronic structure modification are obtained at a specific value for slab separation (z). z=0.36238, which is equivalent to the insulating separation of 13.85 Å, is preferable for free-to-move carriers, while the spin wave maximum is at z=18 Å. The moment observed in the DOS of the CrI3 layer supports an increase in the surface field, which, in turn, explains the effectiveness of the CrI_3 layer in tunneling applications. The CrI3 Fermi surface contains small electronic pockets derived from the Cr-3d doubly degenerate state at M. The doubly degenerate effective mass m^* is approximately constant near the bottom of the nearly free electron band, but the triply m^* increases somewhat at the inflection point by the Cr-3d magnetic field. Depending on the number of d-electrons, the junctions CoMnI3/CrGeTe3, MoI3/CrGeTe3 and WI3/CrGeTe3 are examined. The comparison between CoMnI3, MoI3 and WI3, and CrI3 ensures that the performance of the CrI3 layer is due to the activity of Cr-3d, which provides a unique opportunity to control the junction properties. The DOS shape of the MoI3 layer demonstrates fairly interesting magnetic properties that are nearly similar to those of the CrI3 layer.

INTRODUCTION

Recently, the most modern electronic devices have performed appropriately by combining more than one material layer to improve the device performance [1–4]. The micro-electronics devices show high speed and lower power operation. These advantages are due to the weak bonding between planes, similar to the van der Waals interaction [5]. The distance between nearest neighbor atoms for the in-planes is 1.4 Å. In contrast, the distance between successive planes in the van der Waals heterostructures is 3.35 Å [6–9]. Additionally, these *yz*-layered compounds have nearly free-to-move electrons in the electronic states of Px. That idea of conducting in one direction (*x*-direction) allows for the construction of two-dimensional (2D) layered materials, which show fascinating possibilities [9–11].

The CrI_3 has been extensively studied, providing a new window into magnetic insulators, which are a resource for next-generation topological devices [11–19]. In its equilibrium configuration, a two-dimensional monolayer crystal of CrI_3 is a ferromagnetic semiconductor. However, according to the stacking, two coupled layers may be ferromagnetic or anti-ferromagnetic. A. Leon et al. studied the dependence of the magnetic phase diagram on the strain of the antiferromagnetically coupled bilayer [20,21]. T. Egami et al. have studied the dependence of magnetic moment on layer separation, biaxial strain effects on magnetic and electric properties, first-principle calculations, and the stacking order modification through rotation and transition between the layers [22–25]. Magnon observation for 2D dimensional, interlayer magnetic coupling tune and recent progress of 2D intrinsic ferromagnetic semiconductors in the theoretical side all have been studied for CrI_3 [2,26,27]. Spin-polarized quantum transport properties for sandwich-type Van der Waals magnetic tunnel junctions CrI_3/h-BN/CrI_3 exhibit an interesting odd-even effect within a limited thickness [28–30].

Corresponding author: moaied5@yahoo.com

DOI: 10.21608/ajnsa.2022.150893.1616

However, to the best of our knowledge, $CoMnI_3/CrGeTe_3$, $MoI_3/CrGeTe_3$, and $WI_3/CrGeTe_3$ junctions are strongly related to $CrI_3/CrGeTe_3$, and are still rare to date. The real surfaces are classified into reasonably flat regions called terraces, and losses of a few atomic layers, which change the height, are called steps. Additionally, different orientation terraces relative to the principal surface are named facets, and small surface prominence is referred to as islands. Different degrees of roughness at the contact surface can be caused by fabrication techniques and can also be caused by the layers having different crystal structures. This interface roughness causes potential bumps in the path of the electrons producing scattering to the current carriers. The shape of that interface roughness scattering potential has been described by different models [31]. Starting from the atomistic level until nearby the macroscopic scale, the dynamic evolution of crystal surface is important to understand and control the growth phenomena or surface reconstructions of important materials.

The free-to-move electrons at the interface of layered materials are induced by positive voltage (**E**(x)) towered insulating material, producing tunneling in the interface channel between the metallic and insulating layer. This insulating material works as a potential barrier that forces electrons to tunnel at the interface, such as in MOSFET and Josephson junctions. Since theoretical tools are always used to gain a deeper understanding of the dynamical phenomena on the surface, here we will theoretically study the effect of the distance between the two layers on the electronic properties, starting from the insulating distance (potential barrier) until the van der Waals heterostructures range. These will provide a microscopic explanation for the tunneling efficiency of the $CrI_3/CrGeTe_3$ junction compared to the other studied layers. Additionally, they will establish a better-understood feature of the band structures of specific junctions $CrI_3/CrGeTe_3$, $CoMnI_3/CrGeTe_3$, $MoI_3/CrGeTe_3$, and $WI_3/CrGeTe_3$ through studies on the decisive role of channel thickness or layer separation on the interface scattering potential and tunneling processes.

METHOD OF CALCULATION

A coupled magnetic semiconductor layer $CrI_3/CrGeTe_3$, was derived from the bulk Chromium triiodide. CrI_3 was considered with the experimental lattice constants α=b=6.867 Å and c= 19.807 Å [14]. Additionally, a space group number 148 (R-3) with 3a and 9d site symmetry for atoms Cr and I, respectively, was used in the calculations [14].

The following procedure was used to build up tunneling junctions: we first constructed a 1×2×3 layered supercell structure with CrI_3 monolayers separated by the van der Waals gap, as shown in Figure (1a). The supercell construction produced 7-layers, as shown in Figure (1a). Three layers were removed, and the remaining 4-layers were used to produce the desired construction. Two of the 4-layers were changed from CrI_3 to $CrGeTe_3$, as shown in Figure (1b). This new procedure was sufficient to yield a geometry consisting of slab 1 of $CrGeTe_3$ and slab 2 of CrI_3, resulting in a 2×2 primitive unit cell of CrI_3-$CrGeTe_3$, as shown in Figure (1b).

The calculation was performed on the system with different values for the distance z between the two slabs CrI_3 and $CrGeTe_3$, as shown in Figure (1b). The three times cell repetition along the z-axis or in the c-direction during supercell formation generated sufficient separation (z) between the two slabs to be suitable for the calculations. The maximum allowed z-structure parameter value on the c-direction was found to be 0.61238, equivalent to the divergence of 27.15 Å between slabs on the c-axis. The calculations were performed with a gradual decrease of a 0.1 step in the z-structure parameter, i.e., 0.61238, 0.51238, 0.41238, 0.31238, 0.21238, 0.11238 and 0.06238, which is equivalent to values 27.15 Å to 5 Å with step 4.4333 Å for the z-parameter, as shown in Figure (1b).

Density functional theory (DFT) calculations for CrI_3-$CrGeTe_3$ with deferent junction separations were performed using the full-potential linearized augmented plane wave (FLAPW). The FLAPW had a suitable flat character in the interstitial region in accordance with the junction region. Additionally, the FLAPW had a rapid oscillatory in the core region that was suitable for the slabs internal region. The exchange-correlation was evaluated using the generalized gradient approximation (GGA) with slowly varying densities in PBEsol-GGA, which improves the equilibrium properties of the surfaces of the solid [32]. The muffin tin radii ($R_{M\,T}$) were chosen to minimize the interstitial region. The $R_{M\,T} \times k_{max}$ was set to 7 for the number of plane waves, with l=12 as an expansion of the wave functions inside the muffin tin spheres. The SCF calculations employed a **Γ**-centered grid of 204 **k**−points in the irreducible Brillouin zone taken from a 23x11x3 mesh. The energy and charge convergence criterion was set to 0.001 Ry and 1.1e, respectively, for all values of z.

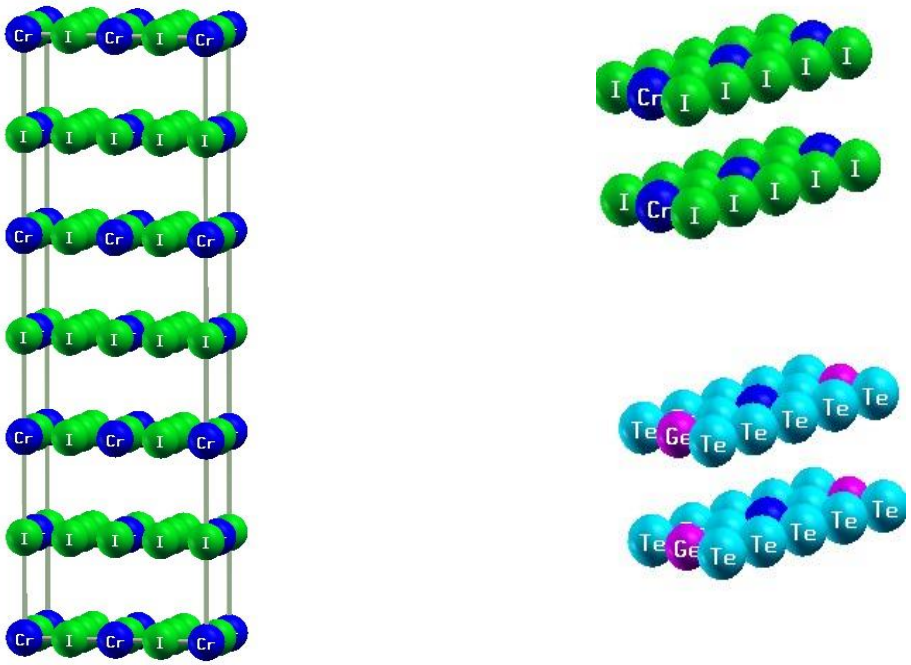

(a) Supercell **(b) Calculated slaps**

Fig. (1): (Color online) The 1×2×3 supercell consists of 24 I and six Cr atoms in the first layer and 24 Te, four Ge, and two Cr atoms in the second layer

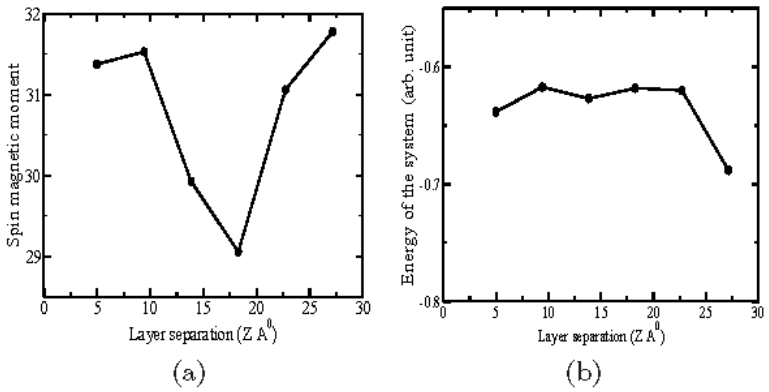

Fig. (2): Magnetic moment versus (a) junction energy (b) slab separation z

RESULTS AND DISCUSSION

The density functional theory (DFT) was used for the interface electronic structure calculations of the heterostructure in Figure (1b). Of particular interest are interfaces between the magnetic half-metallic layer (CrI_3) and the semiconductor layer ($CrGeTe_3$). The CrI_3-$CrGeTe_3$ junction is highly important in spintronic applications. Studying the surface contraction manner of two active layers with a thickness of dielectric inserted between these layers is likely similar to the growth in the *z*-axis. The tunneling probability monotonically increases as the barrier thickness shrinks. The atoms Te, Ge, and I with s and p valence electrons were used for slab formation, in addition to the highly spin-polarized magnetic atom Cr of 6 valence electrons in s and d. The two ideal slabs in Figure (1b) were gradually brought into close contact until the inter-atomic range (*z*= 27.15, 22.7167, 18.2834, 13.8501, 9.4168, 4.9835, and 2.765 Å).

Figure (2a) indicates the relation between the slab separation (z) and the spin magnetic moment. The moment gradually decreases as the two slabs CrI_3 and

$CrGeTe_3$, approach each other, attaining the minimum value for the moment at distance z=18.3 ˚A; the moment then increases as z decrease further. Hence, the magnetic properties of the system are drastically affected by the layer's separations, with magnetic inversion at critical slab separation z=18.3 Å, where the system attained the ability to acquire and maintain an internal dipole moment before and after that critical separation. There is nearly the same as the dipole moment associated with the displacement of atoms away from the center of the point group in the crystal structure.

Figure (2b) displays the system energy as a function of z. The energy of the system is nearly constant in the studied separation range. However, the interaction energy between the slabs begins to decrease at approximately 23 Å.

Electronic structure calculations were conducted for each slab, CrI_3, and $CrGeTe_3$, separately under the same conditions considered for the $CrI_3/CrGeTe_3$ junction. A semiconductor gap was observed for both channel directions of the $CrGeTe_3$ layer, as shown in Figure 6(c, d). Additionally, CrI_3 indicates a half metallicity with semiconductor behavior for the majority of the channel, as shown in Figure 6(a, b). Cr-3d bands indicated by the symbol d in Figure (6a), which extended from -0.3 to -0.6 eV down the Fermi surface at the **Γ** point and nearly at the surface of the Brillouin zone, are indicated by the high symmetry points **M**, **K**, and **A**.

The electronic structure calculations of the $CrI_3/CrGeTe_3$ system show a conductive behavior for different separation values between the slabs. The major shortcomings of the conductive behavior of the junction $Cr_3/CrGeTe_3$ are as follows:

(1) The heterostructure led to the creation of a conductive Kohn-Sham state with energies within the insulator and semiconductor gap for CrI_3 and $CrGeTe_3$, respectively. Where the surface charges interaction rearrangement of the charges in the semiconductor layer ($CrGeTe_3$) produces new energy states in the band structure, as shown in Figure (3). This corresponds with the theory of quantum tunneling, which is a partial propagation of the particle wave function into a forbidden region (energy gap), i.e., the wave function in the barrier region does not equal zero.

(2) The heterostructure layers yield bonds inside the slab that partially satisfy the bonding requirements described for the solids with s and p valence electrons. The elements Ge, Te, and I with 4, 6, and 7 valence electrons, respectively, may form a hybridization or covalent-like quasi bonding between the s and p orbitals or pure directed p bonding that participates in the band structure.

(3) The difference in Fermi energy between the CrI_3 layer and the $CrGeTe_3$ layer generates overlapping between the slab states, so the band structure for the successive z values may appear conductive.

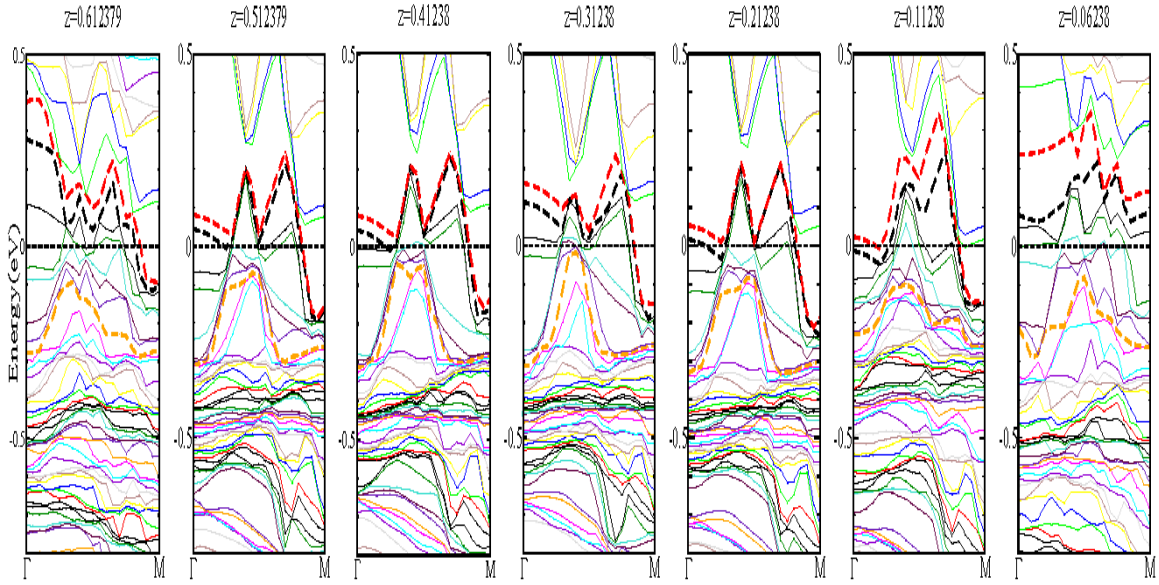

Fig. (3): The topology changes in majority channel band structure of the system $CrI_3/CrGeTe_3$ in the [100] direction with z=0.61238, 0.51238, 0.41238, 0.31238, 0.21238, 0.11238 and 0.06238, which is equivalent to z= 27.15, 22.7167, 18.2834, 13.8501, 9.4168, 4.9835 and 2.765 Å

The challenge of controlling conductivity by electric fields was achieved by the band topology changes as a function of z in Figure (3). These z-changes strongly modify the electronic structure near E_F as follows: The three dashed states, red, black, and orange mostly derived from Cr-3d, as z=0.16238 to z=0.36238, have no crossing to the Fermi level at the **Γ**-point. The location at which the d-band crosses the Fermi level indicates that the bands constitute a low-energy dispersion relation of fermions with d-components. In addition, a free electron state appeared for z=0.36238, 0.46238, and 0.56238, as indicated by the dashed orange d-state in the valance band near E_F. This means that z=0.36238, which is equivalent to slabs separation by 13.85 Å, is preferable for free-to-move carriers. In the upward motion of z values until z=0.21238, a group of Cr-3d bands is separated by a clean slab field and extended to -0.8 eV at the **Γ** point. This group shows a large dispersion for low and high z values.

The significant role of Cr-3d in the magnetic properties and performance of the studied junction led to the analysis of the Cr-3d changes with z inside the junction. Figure (4) indicates the projected DOS changes for Cr-3d with different values of z. The Cr-3d states have a sharp peak at approximately 0.5 eV below the Fermi level. The Figure indicates a ferrimagnetically spin arrangement between the valence states and conduction states. This arrangement decreases the bonding energy because of the difference in the strength of the hybridization between the majority and minority channels. As a result, the Cr-3d states are polarized like f -states. This totally spin-polarized valence and conduction bands led Cr-3d to produce an allowable spin current, which coincides with the experimental observations [33]. This spin wave current is maximum at z=18 Å, as shown in Figure (4). Additionally, Figure (4) indicates a DOS spike of fixed potential for Cr-3d under the Fermi level; its width is about 0.3 eV. The majority of narrow d-bands of the spike are indicated by the symbol d on the energy axis of Figure (6a) at the **Γ** point.

The remaining set of states split from the d-band around point **M** in the valance band is for s-band which is indicated by the ellipses in Figure (6a). These ellipses are closer to the Fermi level for $CrGeTe_3$ in figure 6c than CrI_3 in Figure (6a). When the junction is formed, the surface field acts like a breakdown voltage, destroying these electronic pockets and producing new electronic states. These states have energy in the semiconductor gap energy range. Where, all the s- and d-levels that have the same **K** values are close together, and that would explain the pesky ability of CrI_3 in tunneling applications.

The distinct magnetic properties of the CrI_3 layer led to an examination of other similar layers to explain the magnetic superiority of CrI_3.

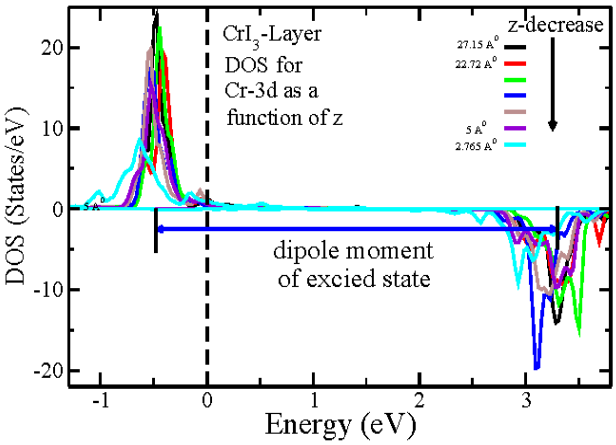

Fig. (4): Density of states in the valence band suffering total flipping in a conduction band

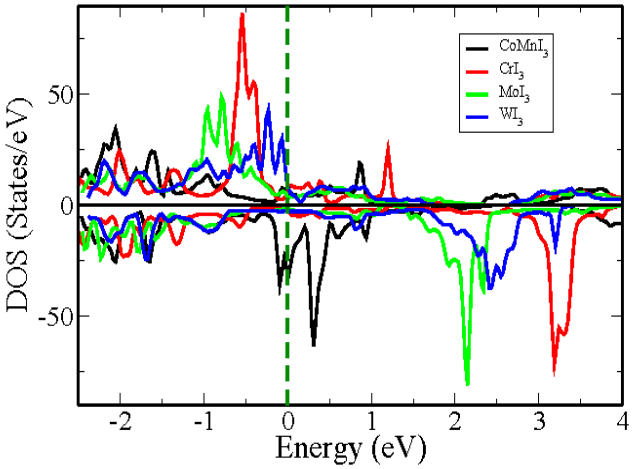

Fig. (5): Total DOS for $CoMnI_3$, CrI_3, MoI_3 and WI_3 layers

The following results are presented in Figure (5), which shows the main DOS differences between the $CoMnI_3$, CrI_3, MoI_3 and WI_3. When the orbital d, which is responsible for the magnetic properties, changes from Cr to W, the sharp peak density decreases, and its energy changes. This trend is due to the band filling of d-electron sub-bands, which increase the d-states, splitting with respect to the Fermi level. The Figure also presents the increase in DOS near the Fermi level, which is the reason for the fascinating magnetic properties of CrI_3 in contrast to the other layers. That remarkable moment in DOS of CrI_3 layer support an increase in the surface field, which

in turn explains the effectiveness of the CrI_3 layer in tunneling applications. Additionally, the increase in DOS is the result of the bonding and antibonding character of d-electron pairs around the Cr-atom. The DOS shape of the MoI_3 layer demonstrates fairly interesting magnetic properties that are nearly similar to those of the CrI_3 layer. The peak intensity and the interval between the valance and conduction peaks of the MoI_3 layer are close to those of the CrI_3-layer, as shown in Figure (5). The highest peak of Mo shifted somewhat towereds the low energy in the conduction and valance bands.

When the junction was formed, the partial DOS (not shown here) explained the imbalance of the directed p-orbital electronic charge of Ge, Te and I in the immediate neighborhood of the interface, creating a dipole moment associated with the presence of the $CrI_3/CrGeTe_3$ junction. That surface p-dipole moment becomes stronger with the formation of the $CrI_3/CrGeTe_3$ junction due to the addition of the moment produced by the Cr-3d, as shown earlier in Figure (4). These dipole moments equate to a Fermi level on either side of the junction because the Fermi level is adjusted by the electrical neutrality of the two layers.

In the case of a large gap, the dipole moment is not sufficient to produce electronic equilibrium. Figure (6) shows a small gap for $CrGeTe_3$ and half metallicity for CrI_3, which could be suitable for the Fermi surface to be balanced on both sides of the studied junction. That would neatly point toward, the properties of the studied heterostructure depend on the changes in energy gap along the reciprocal directions, as indicated in Figure (7b). Thus, considering Figure (6) for the semiconductor layer $CrGeTe_3$, the equilibrium condition may occur at high symmetry points with a small gap, such as at **M** or **K**, but not at **Γ** or **A**. This, in turn, explains the tunnelling behavior of the studied junction.

Consider the ellipses of the valence band electronic pockets at the high symmetry point **M** in Figure (6). These pockets consist of a very small pieces of surfaces that surround the occupied levels and represent a narrow cross-section of the Fermi surface. Interestingly, a weak potential would be enough to destroy those pockets because the energy bands at the high symmetry point **M** of those pockets take the form of the free electron parabola, as shown in Figure (6).

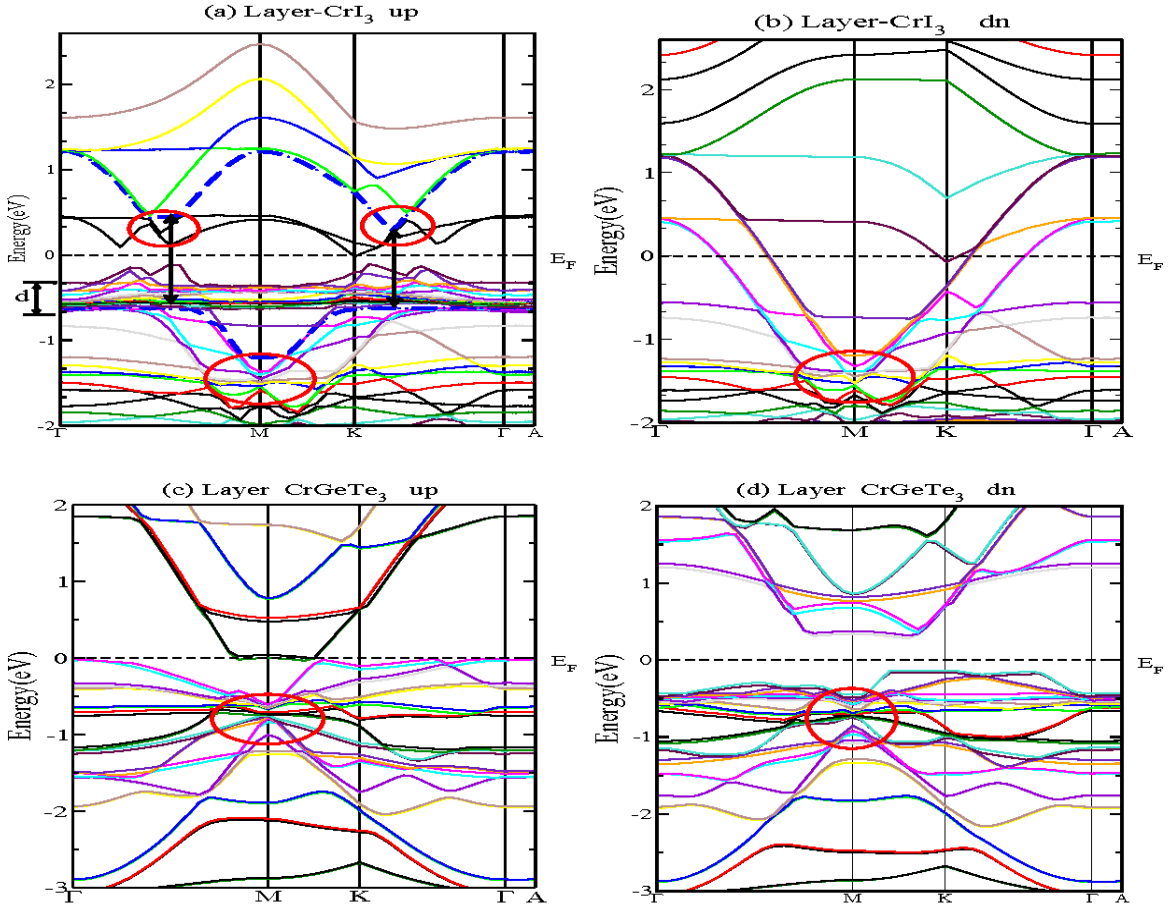

Fig. (6): (a), (b), (c) and (d) show the band structure for the studied layers in the two spin directions

By arguing against conventional band structure, Figure (8), which displays a free electronic state, is separated from the band structure in Figure (6a) for CrI_3. Figure (8) presents a particular way to show the original free electron parabola of the s-level disconnected from the two parabolic sectors that split and form fairly large direct energy gaps in the interior of the Brillouin zone at about k=0.5ΓM and k=0.7ΓK. In the same way, most energy states in Figure (6) can be given a parabola representing the levels of the free electron. Hence, the free electron parabola states prevail in the band structure. Therefore, the application of external weak potential will beat on, not necessarily all, the parabolas of free electrons. These results match the experimental observations [33]. On the other hand, according to the Schottky model, the barrier voltage is proportional to the metal work function. The CrI_3 barrier may be small due to the appearance of nearly free electronic states in the band structure, which is the key for the most promising area of the practical use of the CrI_3-layer. Additionally, the band structure of the magnetic metal layer CrI_3 in Figure 6(a and b) indicates a difference for the majority electrons work function than minority.

The CrI_3-layer shows a characteristic band structure for the majority channel at the Cr-3d orbital, whose width of about 0.3 eV has less conductive activity and nearly has the same behavior at all **K** values. Where, Cr-3d localized states work as a fixed potential under the Fermi level. However, the set of low lying s-electron bands under the d-orbital has a higher activity from -1.5 eV to -0.4 eV and behaves as a free electron for nearly all zone faces **K** values, as indicated in Figure (6). The distinction between the d- and s-bands on one side and the dipole moment field, produced by occupied and empty states, on the other side could be the cause of the special properties of the CrI_3-layer [34–41]. When a junction forms, the excitation of electrons from the valence band to the conduction band of the semiconductor layer $CrGeTe_3$ occurs through new, quasi-bound energy states, as in Figure (3). These states are mostly referred to as the half-metallic layer CrI_3 for most values of k. Furthermore, since the conductivity mainly depends on the states around the Fermi level, conductivity depends on the electronic pockets that produce semi-free electrons moving under the influence of the field of the dipole moment, which is associated with the occupied and empty states of Cr-3d (Figure 4). The band structure diagram shows that those nearly free electrons are allowed in the ΓM and ΓK directions in reciprocal space or the [100] and [110] directions in real space, as shown in Figure (7b).

In summary, Fermi level equilibrium and the small gap and small work function in the KM direction both diminish the conductivity, except in the ΓM and ΓK directions, which in turn produce the tunneling effect, as indicated on the Brillouin zone of Figure (7b). Additionally, the picture outlined above may present a disturbance in the oversimplified Schottky model view of barrier width.

In addition, the effective mass (m^*) is an important parameter for the tunneling current and plays an important role in the dynamics of both electrons and holes, [42,43]. Additionally, m^* has a complicated dependence on the crystallographic directions depending on parabola and non-parabola states on band structure, as in figure 6. Moreover, m^* relies on moment (Figure 4) and state's energy as indicated for the Cr-d states in Figure (6a). It can also have a different magnitude and even different signs, as indicated by Figure (7a). Figure (7a) depicts the effective mass of electron (m^*) considered by its value at the maximum or at minimum for small electronic or small holes pockets. For the conduction electronic state interval from 0.5k until the high symmetry point M and the valance path M → K in Figure (8), each has the same behavior as in Figure (7a).

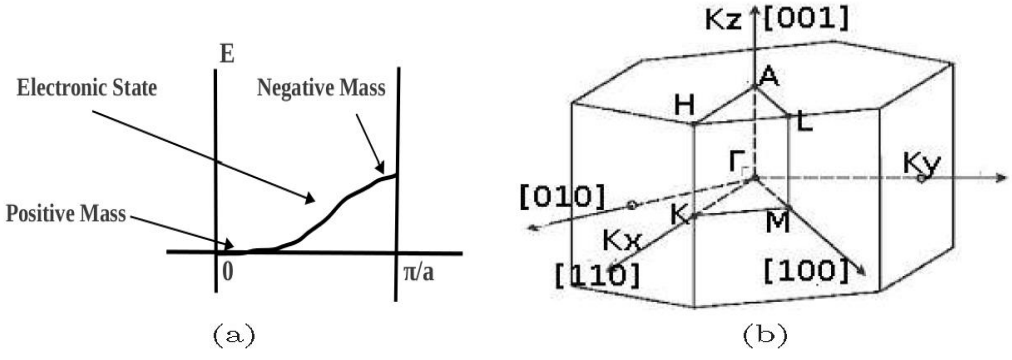

Fig. (7): (a) Schematic drawing of the dispersions near E_F for massless Dirac fermions and massive quasi particles; (b) Brillouin zone for hexagonal structure with high symmetry points and directions in reciprocal space

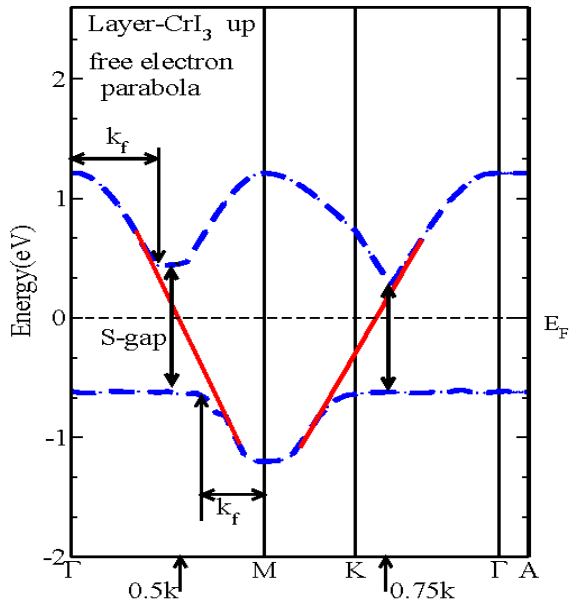

Fig. (8): Zoomed-in view of the free electron parabola state, indicated by the dashed line in Figure (6a)

Consider Figures (6 and 7a); the band structure of the two layers shows a behavior that is the opposite of the effective mass as follows: the m^* of the $CrGeTe_3$-layer, for most conduction states near the Fermi level (E_F), is negative ($m^* < 0$), and the opposite is true for valance states where $m^* > 0$. However, the case is different for CrI_3, where m^* is positive in the valance band. This contrast in the m^* signal facilitates electrical conductions and is one of the unique characteristics of a $CrI_3/CrGeTe_3$ junction.

Near the bottom of the nearly free electron band, the effective mass is approximately constant and can be calculated by the Schrödinger equation:

$$\mathrm{E}(\mathrm{n}, K_x, K_y) = \frac{\pi^2 h^2 n^2}{2m^* Z^2} + \frac{h^2 k_x^2}{2m^*} + \frac{h^2 k_y^2}{2m^*}$$

After that, m^* increases somewhat at the inflection point by the Cr-3d magnetic field, which is indicated in Figure (4), and even becomes negative at the high symmetry points **M** and **K**.

CONCLUSIONS

Electronic structure calculations were performed to elucidate the changes in the physical properties of the $CrI_3/CrGeTe_3$ junction with respect to the separation between the two layers. The magnetic properties of the system were drastically affected by the layer's separations, with magnetic inversion at critical slab separation z=18.3 Å. Where the system could acquire and maintain an internal dipole moment before and after that critical separation. The z-changes strongly modify the electronic structure near E_F . The total spin polarization between the valence and conduction bands led Cr-3d to produce an allowable spin current, which coincides with experimental observations. This spin wave current achieves its maximum at z=18 Å . The remarkable moment in DOS of CrI_3 layer support an increase in the surface field, which in turn explains the effectiveness of the CrI_3 layer in tunneling applications over the other studied layers. The contrast in the m^* signal facilitates electrical conductions and is a unique characteristic of a $CrI_3/CrGeTe_3$ junction. Additionally, this work shows that the layer's separation is a feasible way to adjust the junction properties, which are presumed to be beneficial for technology.

Conflict of Interest

There are no conflicts to declare.

Acknowledgments

The authors acknowledge the computational support provided by Supercomputing Facility in the Bibliotheca Alexandrina, Egypt.

REFERENCES

[1] W.R. Frensley, Chapter 1 - Heterostructure and Quantum Well Physics, in: N.G. Einspruch, W.R. Frensley (Eds.), VLSI Electronics Microstructure Science, Elsevier, 1994: pp. 1–24. https://doi.org/10.1016/B978-0-12-234124-3.50006-9.

[2] Y. Lu, R. Fei, X. Lu, L. Zhu, L. Wang, L. Yang, Artificial Multiferroics and Enhanced Magnetoelectric Effect in van der Waals Heterostructures, ACS Appl. Mater. Interfaces. 12 (2020) 6243–6249. https://doi.org/10.1021/acsami.9b19320.

[3] A. Molina-Sánchez, G. Catarina, D. Sangalli, J. Fernández-Rossier, Magneto-optical response of chromium trihalide monolayers: chemical trends, J. Mater. Chem. C. 8 (2020) 8856–8863. https://doi.org/10.1039/D0TC01322F.

[4] H. Kondo, Y. Akagi, H. Katsura, ${\mathbb{Z}}_{2}$ topological invariant for magnon spin Hall systems, Phys. Rev. B. 99 (2019) 041110. https://doi.org/10.1103/PhysRevB.99.041110.

[5] Y.-P. Wang, M.-Q. Long, Electronic and magnetic properties of van der Waals ferromagnetic semiconductor ${\mathrm{VI}}_{3}$, Phys. Rev. B. 101 (2020) 024411. https://doi.org/10.1103/PhysRevB.101.024411.

[6] A.H. Castro Neto, F. Guinea, N.M.R. Peres, K.S. Novoselov, A.K. Geim, The electronic properties of graphene, Rev. Mod. Phys. 81 (2009) 109–162. https://doi.org/10.1103/RevModPhys.81.109.

[7] Q.H. Wang, K. Kalantar-Zadeh, A. Kis, J.N. Coleman, M.S. Strano, Electronics and optoelectronics of two-dimensional transition metal dichalcogenides, Nature Nanotech. 7 (2012) 699–712. https://doi.org/10.1038/nnano.2012.193.

[8] X. Xu, W. Yao, D. Xiao, T.F. Heinz, Spin and pseudospins in layered transition metal dichalcogenides, Nature Phys. 10 (2014) 343–350. https://doi.org/10.1038/nphys2942.

[9] K.S. Novoselov, A. Mishchenko, A. Carvalho, A.H. Castro Neto, 2D materials and van der Waals heterostructures, Science. 353 (2016) aac9439. https://doi.org/10.1126/science.aac9439.

[10] D. Rhodes, S.H. Chae, R. Ribeiro-Palau, J. Hone, Disorder in van der Waals heterostructures of 2D materials, Nat. Mater. 18 (2019) 541–549. https://doi.org/10.1038/s41563-019-0366-8.

[11] M. Moaied, J. Hong, Tuning the magnetic properties of hydrogenated bilayer graphene and graphene/h-BN heterostructures by compressive pressures, Carbon. 131 (2018) 266–274. https://doi.org/10.1016/j.carbon.2018.01.102.

[12] P. Jiang, C. Wang, D. Chen, Z. Zhong, Z. Yuan, Z.-Y. Lu, W. Ji, Stacking tunable interlayer magnetism in bilayer ${\mathrm{CrI}}_{3}$, Phys. Rev. B. 99 (2019) 144401. https://doi.org/10.1103/PhysRevB.99.144401.

[13] P. Jiang, L. Li, Z. Liao, Y.X. Zhao, Z. Zhong, Spin Direction-Controlled Electronic Band Structure in Two-Dimensional Ferromagnetic CrI3, Nano Lett. 18 (2018) 3844–3849. https://doi.org/10.1021/acs.nanolett.8b01125.

[14] S. Jiang, L. Li, Z. Wang, K.F. Mak, J. Shan, Controlling magnetism in 2D CrI3 by electrostatic doping, Nature Nanotech. 13 (2018) 549–553. https://doi.org/10.1038/s41565-018-0135-x.

[15] B. Huang, G. Clark, D.R. Klein, D. MacNeill, E. Navarro-Moratalla, K.L. Seyler, N. Wilson, M.A. McGuire, D.H. Cobden, D. Xiao, W. Yao, P. Jarillo-Herrero, X. Xu, Electrical control of 2D magnetism in bilayer CrI3, Nature Nanotech. 13 (2018) 544–548. https://doi.org/10.1038/s41565-018-0121-3.

[16] Z. Wu, J. Yu, S. Yuan, Strain-tunable magnetic and electronic properties of monolayer CrI3, Phys. Chem. Chem. Phys. 21 (2019) 7750–7755. https://doi.org/10.1039/C8CP07067A.

[17] K. Hejazi, Z.-X. Luo, L. Balents, Moir\'e magnets, (2020). https://doi.org/10.48550/arXiv.2001.02796.

[18] M. Moaied, J. Hong, Size-Dependent Critical Temperature and Anomalous Optical Dispersion in Ferromagnetic CrI3 Nanotubes, Nanomaterials. 9 (2019) 153. https://doi.org/10.3390/nano9020153.

[19] J.J. Heath, M. Costa, M. Buongiorno-Nardelli, M.A. Kuroda, Role of quantum confinement and interlayer coupling in ${\mathrm{CrI}}_{3}$-graphene magnetic tunnel junctions, Phys. Rev. B. 101 (2020) 195439. https://doi.org/10.1103/PhysRevB.101.195439.

[20] A.M. León, J.W. González, J. Mejía-López, F.C. de Lima, E.S. Morell, Strain-induced phase transition in CrI$\less$sub$\greater$3$\less$/sub$\greater$ bilayers, 2D Mater. 7 (2020) 035008. https://doi.org/10.1088/2053-1583/ab8268.

[21] N. Schulz, A. Chanda, G. Datt, M.V. Kamalakar, T. Sarkar, M.H. Phan, H. Srikanth, Proximity enhanced magnetism at NiFe2O4/Graphene interface, AIP Advances. 12 (2022) 035132. https://doi.org/10.1063/9.0000271.

[22] T. Egami, B.V. Fine, D.J. Singh, D. Parshall, C. de la Cruz, P. Dai, Spin–lattice coupling in iron-pnictide superconductors, Physica C: Superconductivity and Its Applications. 470 (2010) S294–S295. https://doi.org/10.1016/j.physc.2009.11.167.

[23] K. Zollner, P.E.F. Junior, J. Fabian, Strain-tunable orbital, spin-orbit, and optical properties of monolayer transition-metal dichalcogenides, Phys. Rev. B. 100 (2019) 195126. https://doi.org/10.1103/PhysRevB.100.195126.

[24] W. Chen, Z. Sun, Z. Wang, L. Gu, X. Xu, S. Wu, C. Gao, Direct observation of van der Waals stacking–dependent interlayer magnetism, Science. 366 (2019) 983–987. https://doi.org/10.1126/science.aav1937.

[25] D. Soriano, M.I. Katsnelson, J. Fernández-Rossier, Magnetic Two-Dimensional Chromium Trihalides: A Theoretical Perspective, Nano Lett. 20 (2020) 6225–6234. https://doi.org/10.1021/acs.nanolett.0c02381.

[26] J. Cenker, B. Huang, N. Suri, P. Thijssen, A. Miller, T. Song, T. Taniguchi, K. Watanabe, M.A. McGuire, D. Xiao, X. Xu, Direct observation of two-dimensional magnons in atomically thin CrI3, Nat. Phys. 17 (2021) 20–25. https://doi.org/10.1038/s41567-020-0999-1.

[27] Y. Guo, B. Wang, X. Zhang, S. Yuan, L. Ma, J. Wang, Magnetic two-dimensional layered crystals meet with ferromagnetic semiconductors, InfoMat. 2 (2020) 639–655. https://doi.org/10.1002/inf2.12096.

[28] Z. Yan, R. Zhang, X. Dong, S. Qi, X. Xu, Significant tunneling magnetoresistance and excellent spin filtering effect in CrI3-based van der Waals magnetic tunnel junctions, Phys. Chem. Chem. Phys. 22 (2020) 14773–14780. https://doi.org/10.1039/D0CP02534H.

[29] F. Subhan, M.U. Farooq, J. Hong, Bias-dependent transport properties of passivated tilted black phosphorene nanoribbons, Phys. Chem. Chem. Phys. 20 (2018) 11021–11027. https://doi.org/10.1039/C8CP00090E.

[30] F. Subhan, J. Hong, Bias dependent transport property of defective hydrogen passivated tilted black phosphorene nanoribbon, Physica E: Low-Dimensional Systems and Nanostructures. 105 (2019) 151–155. https://doi.org/10.1016/j.physe.2018.09.012.

[31] E. Kaxiras, Atomic and Electronic Structure of Solids, Cambridge University Press, Cambridge, 2003. https://doi.org/10.1017/CBO9780511755545.

[32] J.P. Perdew, A. Ruzsinszky, G.I. Csonka, O.A. Vydrov, G.E. Scuseria, L.A. Constantin, X. Zhou, K. Burke, Restoring the Density-Gradient Expansion for Exchange in Solids and Surfaces, Phys. Rev. Lett. 100 (2008) 136406. https://doi.org/10.1103/PhysRevLett.100.136406.

[33] L. Chen, J.-H. Chung, T. Chen, C. Duan, A. Schneidewind, I. Radelytskyi, D.J. Voneshen, R.A. Ewings, M.B. Stone, A.I. Kolesnikov, B. Winn, S. Chi, R.A. Mole, D.H. Yu, B. Gao, P. Dai, Magnetic anisotropy in ferromagnetic ${\mathrm{CrI}}_{3}$, Phys. Rev. B. 101 (2020) 134418. https://doi.org/10.1103/PhysRevB.101.134418.

[34] G. Menichetti, M. Calandra, M. Polini, Electronic structure and magnetic properties of few-layer Cr $\less$sub$\greater$2$\less$/sub$\greater$ Ge $\less$sub$\greater$2$\less$/sub$\greater$ Te $\less$sub$\greater$6$\less$/sub$\greater$: the key role of nonlocal electron–electron interaction effects, 2D Mater. 6 (2019) 045042. https://doi.org/10.1088/2053-1583/ab2f06.

[35] D.R. Klein, D. MacNeill, Q. Song, D.T. Larson, S. Fang, M. Xu, R.A. Ribeiro, P.C. Canfield, E. Kaxiras, R. Comin, P. Jarillo-Herrero, Enhancement of interlayer exchange in an ultrathin two-dimensional magnet, Nature Physics. 15 (2019). https://doi.org/10.1038/s41567-019-0651-0.

[36] Y.-J. Sun, S.-M. Pang, J. Zhang, Review of Raman spectroscopy of two-dimensional magnetic van der Waals materials\ast, Chinese Phys. B. 30 (2021) 117104. https://doi.org/10.1088/1674-1056/ac1e0f.

[37] D. Soriano, C. Cardoso, J. Fernández-Rossier, Interplay between interlayer exchange and stacking in CrI3 bilayers, Solid State Communications. 299 (2019) 113662. https://doi.org/10.1016/j.ssc.2019.113662.

[38] H. Li, S. Ruan, Y.-J. Zeng, Intrinsic Van Der Waals Magnetic Materials from Bulk to the 2D Limit: New Frontiers of Spintronics, Advanced Materials. 31 (2019) 1900065. https://doi.org/10.1002/adma.201900065.

[39] N. Ubrig, Z. Wang, J. Teyssier, T. Taniguchi, K. Watanabe, E. Giannini, A.F. Morpurgo, M. Gibertini, Low-temperature monoclinic layer stacking in atomically thin CrI$\less$sub$\greater$3$\less$/sub$\greater$ crystals, 2D Mater. 7 (2019) 015007. https://doi.org/10.1088/2053-1583/ab4c64.

[40] N. Sivadas, S. Okamoto, X. Xu, Craig.J. Fennie, D. Xiao, Stacking-Dependent Magnetism in Bilayer CrI3, Nano Lett. 18 (2018) 7658–7664. https://doi.org/10.1021/acs.nanolett.8b03321.

[41] C. Gong, X. Zhang, Two-dimensional magnetic crystals and emergent heterostructure devices, Science. 363 (2019) eaav4450. https://doi.org/10.1126/science.aav4450.

[42] D. König, M. Rennau, M. Henker, Direct tunneling effective mass of electrons determined by intrinsic charge-up process, Solid State Electronics. 51 (2007) 650–654. https://doi.org/10.1016/j.sse.2007.03.009.

[43] B. Brar, G.D. Wilk, A.C. Seabaugh, Direct extraction of the electron tunneling effective mass in ultrathin SiO2, Appl. Phys. Lett. 69 (1996) 2728–2730. https://doi.org/10.1063/1.117692.